Experimental and numerical study of electrically-driven MHD flow in a modified cylindrical annulus: (1) Base flow

Zacharias Stelzer,[1] David Cébron,[1, 2] Sophie Miralles,[1] Stijn
Vantieghem,[1] Jérôme Noir,[1] Peter Scarfe,[1] and Andrew Jackson[1]

[1]*Institute of Geophysics, ETH Zürich, Switzerland*
[2]*Université Grenoble Alpes, CNRS, ISTerre, Grenoble, France*

Shear layers in confined liquid metal MHD flow play an important role in geo- and astrophysical bodies as well as in engineering applications. We present an experimental and numerical study of liquid metal MHD flow in a modified cylindrical annulus that is driven by an azimuthal Lorentz force resulting from a forced electric current under an imposed axial magnetic field. Hartmann and Reynolds numbers reach $M_{max} \approx 2000$ and $Re_{max} \approx 1.3 \cdot 10^4$, respectively, in the steady regime. The peculiarity of our model geometry is the protruding inner disk electrode which gives rise to a free Shercliff layer at its edge. The flow of liquid GaInSn in the experimental device ZUCCHINI (ZUrich Cylindrical CHannel INstability Investigation) is probed with ultrasound Doppler velocimetry.

We establish the base flow in ZUCCHINI and study the scaling of velocities and the free Shercliff layer in both experiment and finite element simulations. Experiment and numerics agree well on the mean azimuthal velocity $u_\phi(r)$ following the prediction of a large-M theoretical model. The large-M limit, which is equivalent to neglecting inertial effects, appears to be reached for $M \gtrsim 30$ in our study. In the numerics, we recover the theoretical scaling of the free Shercliff layer $\delta_S \sim M^{-1/2}$ whereas δ_S appears to be largely independent of M in the experiment.

I. INTRODUCTION

Magnetohydrodynamics (MHD) is the subject concerned with the interplay of electrically conducting fluids and magnetic fields. Interest in MHD arises from geo- and astrophysical contexts as well as from engineering applications. In the field of geo- and astrophysics, Larmor [1] proposed an MHD dynamo to explain the generation of magnetic fields in the Sun and the Earth almost a century ago. Today this theory is widely accepted and supported by numerical and experimental evidence; for a review see Olson [2].

In the area of engineering, the advent of liquid metal MHD came with Hartmann's invention of the electromagnetic conduction pump around 1915 [3] and his two seminal articles on 'Hg dynamics' [4, 5]. Since then MHD has found various applications in metallurgy and material processing, liquid metal blankets of fusion reactors as well as electromagnetic flow meters and pumps [6].

An important parameter characterizing the dynamical regime of liquid metal experiments is the Reynolds number

$$Re = \frac{U_0 a}{\nu}, \tag{1}$$

where ν is the kinematic viscosity, a and U_0 are typical length and velocity scales, respectively. The effects of the magnetic field are measured by the Hartmann number, defined as

$$M = aB_0\sqrt{\frac{\sigma_e}{\rho\nu}} \tag{2}$$

where B_0 is the imposed magnetic field strength, ρ the mass density and σ_e the conductivity of the fluid. Strong

magnetic fields ($M \gg 1$) tend to make the flow uniform (quasi-2D) along the direction of the field **B**. The presence of walls perpendicular and parallel to **B** leads to Hartmann and Shercliff layers (also called 'side layers'). The thickness of these layers scales as $\delta_H \sim M^{-1}$ and $\delta_S \sim M^{-1/2}$ respectively for large M [4, 7].

A special case of liquid metal MHD is the 'quasi-static' limit where induced magnetic fields are negligible. It is characterized by small $Rm \lesssim 1$ and $S \lesssim 1$. Here Rm and S denote the magnetic Reynolds and the Lundquist number, respectively, which are defined as $Rm = \mu_0\sigma_e U_0 a$ and $S = (\mu_0/\rho)^{1/2}\sigma_e a B_0$ with $\mu_0 = 4\pi \cdot 10^{-7}$ Hm^{-1} the permeability of free space.

Since the pioneering work of Hartmann, various studies considered laminar pressure-driven MHD flow in straight channels and ducts subject to different electrical boundary conditions [7–10]. Using a boundary-layer technique, Hunt and Stewartson [9] studied a duct with walls perpendicular to **B** being electrically insulating and parallel walls conducting, and derived expressions for the flow rate in the form of an asymptotic expansion in the limit of large M (neglecting secondary flows). Amongst other setups, they considered the purely electrically-driven case of an MHD pump, which is also the driving mechanism in our setup.

In order to avoid entrance effects which are always present in straight duct experiments, other studies employed closed geometries like cylindrical ducts or spherical shells. Following the narrow-gap experiment of Baylis [11], Baylis and Hunt [12] performed the first concise study of flow in a cylindrical annulus with rectangular cross section. Walls perpendicular to **B** were again electrically insulating, parallel walls were conducting in order to impose a radial current. Baylis and Hunt [12] worked in the large-M limit in order to neglect secondary (radial

and axial) flows. Their condition for inertial effects to be negligible was $\left(K/M^2\right)^2 \lambda \ll 1$ with the Dean number $K = \lambda^{1/2} Re$ measuring curvature effects and the curvature ratio $\lambda = d/2r_m$ of channel half-width $d/2$ to mean radius r_m. Under these assumptions, they found an expression for the azimuthal velocity in the core of the flow,

$$u_\phi^{BH}(r) = \frac{I}{4\pi r \sqrt{\sigma_e \rho \nu}}, \qquad (3)$$

where I is the electrical current forcing the flow, and r is the radial coordinate. In their theoretical model, Baylis and Hunt [12] additionally took into account the Hartmann and side layers. By comparing the resulting flow rate with experimental data from Baylis [13], they confirmed the asymptotic theory for the side layer from Hunt and Stewartson [9].

A further theoretical study of laminar MHD flow in annular ducts with rectangular cross section was undertaken by Tabeling and Chabrerie [14]. Using a boundary-layer technique, they focused on the secondary flows, which Baylis and Hunt [12] had neglected, in the high-M regime. Tabeling and Chabrerie [14] employed a perturbation method containing expansions in ascending powers of the curvature ratio λ. They derived the velocities in the core and the Hartmann layers, and found that secondary flows in these regions are dominantly one-dimensional (suppression of u_z). For the side layers, secondary flows are far more intense. The secondary flow structure and the number of eddies in the side layer depends on the conductivities of the walls. The expansion in terms of ascending powers of λ in the perturbation method of Tabeling and Chabrerie [14] converges if $K/M^{5/4} \ll 1$ which is a more stringent criterion for inertial effects to be negligible than the one in [12].

Numerical studies of quasi-static MHD flow in cylindrical geometries were performed using direct numerical simulation [15–17]. Other authors employed an effective 2D model for low-Rm MHD flows which conveniently incorporates boundary layer and recirculation effects [18, 19]. We will reference these studies in more detail in the follow-up paper termed 'Paper 2' which addresses instabilities and flow transitions in our experiment.

In recent years, there have been at least three experimental studies of electrically-driven MHD flow in cylindrical annuli: Moresco and Alboussière [20] studied the stability of the Hartmann layer which we will come back to in Paper 2. Boisson *et al.* [21] observed travelling waves in a narrow-gap annulus. Mikhailovich *et al.* [22] studied the decay of mean velocity components and turbulent fluctuations. All of these experiments have in common with Baylis and Hunt [12] the simple geometry with straight conducting side walls.

In contrast, ZUCCHINI features modified cylindrical side walls with a prominent disk electrode at the inner cylinder and a ring electrode at the outer one, coloured in Figure 1; all remaining walls are insulating. This gives
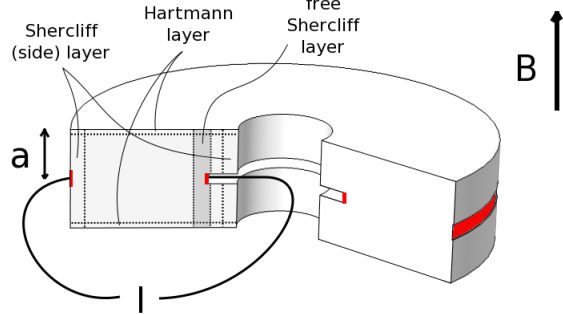

FIG. 1. Sketch of the modified cylindrical annulus ZUCCHINI. Forcing an axisymmetric electrical current I through the liquid metal under an imposed magnetic field **B** gives rise to a Lorentz force which drives an azimuthal flow. The electrodes are coloured in red, the remaining walls are insulating. The half-height a is used as length scale in the nondimensionalization.

rise to a free shear/Shercliff layer at the edge of the disk electrode. In this respect, our experiment is more similar to the MATUR experiment of Messadek and Moreau [23] who studied the quasi-2D turbulent behaviour occuring in cylindrical shear flow resulting from the injection of electrical current in the bottom plate.

An overview of the dimensions and parameters of the previous experiments and ZUCCHINI is given in Table I; the latter reaches Hartmann numbers that are more than double the ones of the other experiments. Another novel feature of our experiment is that we employ two UDV probes which enable us to recover profiles of radial and chordwise velocities through the free shear layer as well as the radial profile of mean azimuthal velocity in the core flow.

ZUCCHINI serves as a prelude to an experiment of electrically-driven liquid sodium flow in a rapidly rotating spherical shell along the lines of Hollerbach *et al.* [24]. The latter with its tentative acronym SpiNaCH is designed to study the 'magnetostrophic regime', i.e. a balance between Coriolis and Lorentz forces, which is believed to govern the motions of liquid metal in the Earth's outer core.

The present paper focuses on the steady and axisymmetric base flow in ZUCCHINI; instabilities will be considered in the follow-up Paper 2. We describe the physical model underlying this work in Section II. In the subsequent Section III, we detail the numerical and experimental setup as well as the methods. The results Section IV is subdivided into the order-one azimuthal flow, the recirculation flow and the shear layers. In Section V, we discuss differences between the numerical and experimental models.

TABLE I. Parameter values of relevant experimental studies. Height $h = 2a$, outer radius r_o and width d of duct, maximum magnetic field strength B_{max}, as well as resulting maximum Hartmann number M^*_{max} and liquid metal used. Note: For comparison, the definition of the Hartmann number used in this table is $M^* = 2M$, double the Hartmann number M from Equation 2 used throughout the paper, since M^* was reported in the previous studies. Hg means mercury, PD(P) potential difference (probes) which are not shown in this study.

	h in cm	r_o in cm	d in cm	B_{max} in T	M^*_{max}	I in A	fluid	measurements
Baylis [11]	5	2.7	0.12	0.5	15	up to 30	Hg	global PD
Baylis [13]	0.39-3.1	7	0.39-3.1	0.4	128	0.1-110	Hg	global PD
Moresco and Alboussiere [20]	1	5	1	13	1690	650	Hg	global PD, pressure
Boisson *et al.* [21]	12	4	1.2	0.15	460	50	GaInSn	UDV
Mikhailovich *et al.* [22]	6.25	3.525	3.125	0.125	160	120	GaInSn	local PDP
Messadek and Moreau [23]	1	11	11	6	1800	10-70	Hg	local PDP
ZUCCHINI (this work)	10	20.5	16	1	4000	300	GaInSn	UDV, local PDP

II. MODEL DESCRIPTION

The physical model studied here by numerical simulations and laboratory experiments is a cylindrical annulus filled with an electrically conducting fluid. The basic setup is shown in Figure 1. Container and fluid are subject to an imposed axial magnetic field $\mathbf{B} = B_0 \mathbf{e}_z$ with a strength of up to 1 T. We force an electrical current I of up to 300 A between the edge of the disk electrode at the center and the ring electrode at the outer cylinder. The remaining walls of the container are electrically insulating. The radial current in an axial magnetic field gives rise to a Lorentz force $\mathbf{f}_L = \mathbf{j} \times \mathbf{B}$ in an azimuthal direction resulting in an azimuthal fluid flow.

The governing equations of the system are the Navier-Stokes equation including the Lorentz force $\mathbf{f}_L$, the incompressible continuity equation, Ohm's law and the equation of charge conservation,

$$\rho \left(\frac{\partial \mathbf{u}}{\partial t} + \mathbf{u} \cdot \nabla \mathbf{u} \right) = -\nabla p + \rho \nu \nabla^2 \mathbf{u} + \mathbf{j} \times \mathbf{B} \quad (4)$$

$$\nabla \cdot \mathbf{u} = 0 \quad (5)$$

$$\mathbf{j} = \sigma_e \left(\mathbf{E} + \mathbf{u} \times \mathbf{B} \right) \quad (6)$$

$$\nabla \cdot \mathbf{j} = 0, \quad (7)$$

where $\mathbf{u}$ is the velocity, $\mathbf{E}$ is the electric field and p is the pressure. We are working in the quasi-static approximation ($Rm, S \lesssim 1$) where induced magnetic fields are negligible and the field is entirely given by the imposed field $\mathbf{B}$. In this case, $\nabla \times \mathbf{E} = -\partial \mathbf{B}/\partial t = 0$, so that the electric field can be written as the gradient of a potential Φ, i.e. $\mathbf{E} = -\nabla \Phi$.

Charge conservation (Eq. 7) can be exploited to eliminate the current density $\mathbf{j}$ from Ohm's law (Eq. 6). In contrast to the full MHD equations, the system then only contains one electromagnetic variable. Following this path and using the half-height a, the imposed magnetic field strength B_0 and a typical velocity U_0 as scales,

Equations 4-7 are rewritten in nondimensional form,

$$\frac{Re}{M^2} \left(\frac{\partial \mathbf{u}}{\partial t} + \mathbf{u} \cdot \nabla \mathbf{u} \right)$$

$$= -\nabla p + \frac{1}{M^2} \nabla^2 \mathbf{u} + (-\nabla \Phi + \mathbf{u} \times \mathbf{B}) \times \mathbf{B} \quad (8)$$

$$\nabla \cdot \mathbf{u} = 0 \quad (9)$$

$$\nabla^2 \Phi = \nabla \cdot (\mathbf{u} \times \mathbf{B}). \quad (10)$$

The nondimensional parameters governing the system are the Hartmann number M (Eq. 2) and the Reynolds number (Eq. 1). The square of the Hartmann number M^2 gives the ratio of Lorentz to viscous forces. The Reynolds number Re is the ratio of inertial to viscous forces. Alternatively the interaction parameter $N = M^2/Re$ can be used in the nondimensionalization which gives the ratio of Lorentz to inertial forces.

III. METHODS

A. Numerical simulation

We perform numerical simulations using the commercial finite element (FE) code Comsol Multiphysics (version 4.3b) in order to gain a detailed insight into the structure of the base flow encountered in the experiment. The FE method facilitates the implementation of complex geometries.

The system of equations to be solved in the geometry of our modified cylindrical annulus is given in Equations 8-10 with $\mathbf{B} = \mathbf{e}_z$. In the first step (this paper), we are only interested in the base flow, which in ZUCCHINI is assumed to be steady and axisymmetric. Hence we choose to perform axisymmetric simulations ($\partial/\partial\phi = 0$) of a cross-section in the (r, z)-plane, but allowing for non-zero u_ϕ; such calculations are often referred to as 2D3C (2 dimensions, 3 components) simulations.

The governing equations need to be amended with mechanical as well as electrical boundary conditions. The

mechanical boundary condition for all walls is no slip, $\mathbf{u} = \mathbf{0}$. For the electrical boundary conditions, we choose $-\nabla\Phi = \mathbf{e_r}$, which means that we impose the electric current density j_0 at the inner electrode. The outer electrode is set to ground, $\Phi = 0$. A detailed reasoning for this choice is given in Appendix A. The remaining walls are insulating and have to fulfill the dimensionless electrical boundary condition $-\mathbf{n} \cdot \nabla\Phi = 0$. The initial conditions are $\mathbf{u} = \mathbf{0}$ and $p, \Phi = 0$ in the whole geometry.

The model geometry is a cross-section in the (r, z)-plane of the container chosen to be as close to the experimental setup as possible meaning that it has the same shape and aspect ratio. Two minor differences have been introduced. The first is that in the numerics also the outer electrode protrudes from the wall for reasons of generality whereas in the experiment it is mounted flush. Translated into dimensional units, however, this modification amounts to only 1 mm of prominence. The second point consists in a specified rounding of the electrode edges with a curvature radius of 0.5 mm (dimensionalized) in the numerics. The amount of rounding on the experimental disk electrode might in fact be of similar size. This modification with conducting boundary conditions was found to yield a higher degree of charge conservation.

As a result of the convergence study presented in Appendix B where mainly the order of discretization and the mesh size were varied, we use Lagrange elements of order three for the discretization of the velocity, order two for the pressure, and quintic elements for the electrical potential. The mesh is triangular and quadrilateral in the core and the boundary layers, respectively. A drawback is the fact that charge is not automatically conserved using Lagrange elements.

We conduct a parameter study varying the Hartmann number M and the input parameter $Re_i = j_0 a(\nu\sigma B_0)^{-1}$ over two to three orders of magnitude, $M = \{1, 3, 10, 20, 50, 100, 150, 200\}$ and $Re_i = \{1, 3, 10, 30, 100, 300, 1000\}$ resulting in 56 parameter combinations. The numerical model consists of 25308 domain elements and 900 boundary elements, and has roughly 10^6 degrees of freedom. The advantage of 2D3C simulations is that they can be run on a single node with every model running for less than 2 CPU hours. After applying the quality criteria from Appendix B, we are left with 51 models which have all reached a steady state solution, $\partial/\partial t = 0$.

The velocities from the numerical simulations presented in Section IV are averages over lines or different volumes like the core flow or the boundary layers where we assumed the theoretical scalings of the Hartmann and Shercliff layers. Volume averages are either computed as

$$\langle u_\phi \rangle = \frac{\iiint u_\phi(r, z)\, r\mathrm{d}r\mathrm{d}\phi\mathrm{d}z}{\iiint r\mathrm{d}r\mathrm{d}\phi\mathrm{d}z}, \tag{11}$$

or based on kinetic energies as

$$\|u_r\| = \left(\frac{\iiint u_r^2(r, z)\, r\mathrm{d}r\mathrm{d}\phi\mathrm{d}z}{\iiint r\mathrm{d}r\mathrm{d}\phi\mathrm{d}z} \right)^{1/2}. \tag{12}$$

The second definition is applied for the radial velocity component u_r because it changes sign within the volume.

B. Laboratory experiment

The ZUCCHINI experiment is designed to study electrically-driven MHD flow in a modified cylindrical annulus. In this paper, we are interested in the base flow; the instabilities that develop in the free shear layer at the edge of the inner electrode are the scope of Paper 2.

1. Setup

The experimental setup of ZUCCHINI consists of three essential parts: the tank itself, the coils creating the magnetic field and the current supply. Moreover we use an argon overpressure in the container to keep the working liquid GaInSn pure, and ultrasonic Doppler velocimetry (UDV) to diagnose the flow.

The ZUCCHINI container has an inner height of $h = 2a = 10$ cm (cf. Fig. 1). The radii of the inner and outer cylinders are $r_i = 4.5$ cm and $r_o = 20.5$ cm respectively. The disk electrode protruding from the inner cylinder has a radius of $r_d = 7.5$ cm, its axial width is 1 cm. The ring electrode along the outer cylinder is 1.5 cm wide and consists of six segments separated by small gaps.

During our experiments, we employed two different coil systems for the generation of the magnetic field. For the lower magnetic field strengths up to 0.1 T, we used a modified Helmholtz coil system with three resistive copper coils manufactured by Caylar ('Caylar' setup). The field strength was measured by two calibrated Hall probes with a precision of < 0.1 mT on the top lid of the container. For the higher fields up to 1 T, we employed a single superconducting coil from Cryomagnetics, Inc. ('Cryo' setup). The two systems also differ slightly in the field geometry. The 'Caylar' setup creates a roughly uniform field within the tank volume which decreases in strength by only 7% with the radius. The 'Cryo' setup is characterized by increasing field strengths with radius and a finite amount of field curvature near the outer cylinder.

The forcing current I between inner and outer electrodes is generated by power supplies of type SM 18-50 from Delta Elektronika. These have an output voltage of 0-18 V and an output current of 0-50 A. They are characterized by an rms ripple and noise as low as 5 mA. In our first setup 'Caylar' ($B_{max} = 0.1$ T), we employ three power supplies resulting in $I_{max} = 150$ A, while for the 'Cryo' setup ($B_{max} = 1$ T), we double the number of power supplies to reach $I_{max} = 300$ A (cf. Tab. III). Details about the current distribution are discussed in Section V A.

The container is filled with 12.5 l (80 kg) of the eutectic alloy GaInSn. We use MCP 11 alloy from 5N Plus

TABLE II. Physical properties of GaInSn from Morley *et al.* [25]. We present the data set resembling most the MCP11 alloy from 5N Plus used in our setup.

kinematic viscosity ν	$2.98 \cdot 10^{-7}$ m^2/s
electrical conductivity σ_e	$3.1 \cdot 10^6$ $(\Omega\mathrm{m})^{-1}$
density ρ	6360 kg/m^3
melting point T_m	10.5°C
sound speed c	2730 m/s

FIG. 2. Top view of tank with orientation of UDV probes R (radial) and X (chordwise) in red. The angle α of the chordwise beam with the radial direction decreases with the distance from probe 2.

UK Ltd. According to the certificate of analysis, it contains 65.9% gallium, 20.8% indium and 13.3% tin. Table II gives its relevant physical properties. Besides being liquid at room temperature, GaInSn has the advantage of not being hazardous to human health and the environment. It may, however, be corrosive to metals, it weakens especially aluminium, and it is expensive. Additionally it is easily oxidized forming a sludge from mainly gallium oxides (Ga$_2$O$_3$, Ga$_2$O) which degrades or precludes experimental measurements.

Prior to the first filling, the tank is thoroughly cleaned with isopropyl alcohol, and the GaInSn is kept under a slight overpressure of argon in a storage tank [25, 26]. The tubes and the experimental cavity are flushed with argon. Once the GaInSn is transferred, a permanent overpressure of 0.2 bar of argon is maintained to avoid contamination. In addition, during the first filling the GaInSn is filtered through four meshes of 100, 50, 30 and 15 μm to remove oxides. Around 90% of the sludge stays in the coarsest mesh, and after the 50 μm mesh, hardly any sludge remains. Over the several months of experiments it was never necessary to empty and clean the GaInSn, both electrical and acoustic couplings remaining very good.

2. Measurements

The flow in ZUCCHINI is diagnosed with Ultrasonic Doppler Velocimetry (UDV). The temperature of the tank is monitored by a K-type thermocouple mounted on the central disk electrode.

UDV as used in our experiment is based on the pulsed emission of ultrasonic waves that are reflected at particles in the fluid. Velocities are derived from shifts in position between pulses resulting in a profile of the velocity component along the ultrasound beam. We use a DOP3010 box from Signal Processing S.A., and multiplex two channels. The emitting frequency f_e of the probes is selected according to the desired maximum profile depth p_{max} and velocity v_{max} which are related by

$$p_{max}v_{max} = \frac{c^2}{8f_e} \qquad (13)$$

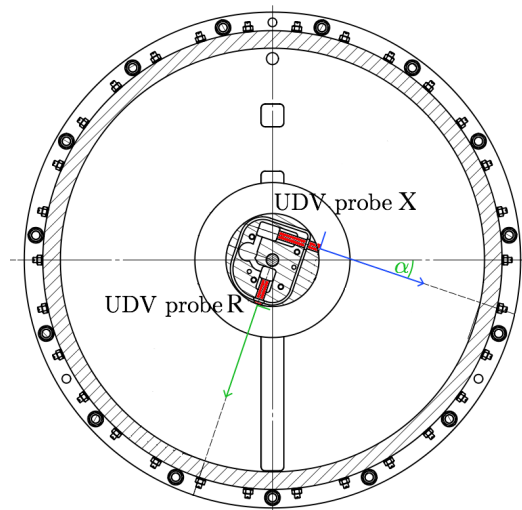where c is the speed of sound (cf. Table II) in the fluid [27]. We use two UDV probes with $f_e = 8$ MHz to achieve sufficient resolution. The wave length in GaInSn is 0.34 mm. The maximum achievable velocity measurement in ZUCCHINI is of the order of 1 m/s which is sufficient since we do not measure u_ϕ directly. The half-angle of divergence of the ultrasonic beam is 4.8°. The near field characterized by corrupted signals goes up to 1.8 cm distance from the probe.

The probes are pointing outwards from the inner cylinder in a horizontal plane 2.1 cm above the central plane of the tank. Probe R ('radial') is measuring purely the radial velocity u_r along a radial profile. Probe X ('chordwise') has an offset of 90° to probe R in azimuthal direction, and points outward forming a skew angle with the radial rays intersecting it as seen in Figure 2. It measures u_χ, a combination of u_r and u_ϕ, with a respective contribution that depends on the location along the profile. This is exploited to construct radial profiles of mean azimuthal velocity u_ϕ in the next section.

Measurements with UDV in liquid metals have become feasible in the last decades, for instance it was used in gallium [28]. We rely on the unavoidable oxides in GaInSn as scatterers of the ultrasonic beam, mainly Ga$_2$O$_3$ (6440 kg/m^3) and GaO$_2$ (4770 kg/m^3) [21, 29, 30]. Some previous studies used UDV through the container wall [21, 28], others brought the probes in direct contact with the GaInSn as is done in our experiment [30]. A good mixing of the oxides in GaInSn is essential.

A typical experimental run begins by ramping up the current in the magnetic coils. The fluid and the oxides are mixed up by a strong electrical current through the tank, typically 150 A or more. After the fluid has come to rest, we record with UDV at a given magnetic field strength stepwise increasing the electrical current. Before any recording, we let the flow reach its new equilib-

TABLE III. Overview of the measurements taken in the two setups 'Caylar' and 'Cryo'. $\#(B)$ gives the number of sweeps of $I \in [I_{min}, I_{max}]$ performed in the range $B \in [B_{min}, B_{max}]$; **B** describes the geometry of the field.

	B_{min}	B_{max}	$\#(B)$	**B**	I_{min}	I_{max}
'Caylar'	17.5 mT	83.4 mT	5	$\partial B_{r,z}/\partial r \lesssim 0$	0 A	150 A
'Cryo'	83.5 mT	1000 mT	9	$\partial B_{r,z}/\partial r > 0$	0 A	300 A

rium state. The settling time decreases with increasing magnetic field and current.

The sampling rate of the UDV is adjusted according to signal quality and the ability to resolve the observed oscillations (scope of Paper 2). In general it increases from ~ 1 Hz at low forcing current to ~ 30 Hz at 150-300 A. The recording time is set such that the frequency resolution is sufficient (~ 0.01 Hz for the oscillations). It decreases from ~ 150 s to ~ 60 s with increasing current.

The parameter values of the recordings are given in Table III. As a consistency check for our data set, we took measurements at $B = 83.5$ mT ($M = 169$) in both the 'Caylar' and the 'Cryo' setup. The mean azimuthal flow $u_\phi(r)$ turns out to be similar in magnitude and also in structure. This allows us to combine the two data sets despite the differing magnetic fields in the two setups. For the base flow studied in this paper, the 'Cryo' data set provides more data due to its larger M. The first instability is not observed below a forcing current of roughly 10 A at $M = 2022$, while the flow is already unstable at 2 A for moderate M in the 'Caylar' setup.

3. Processing

Experimental velocities presented in Section IV are temporal means of the values u_i measured by UDV where $i \in \{r, \chi, \phi\}$. Since we operate in the steady regime, deviations from the mean $\overline{u}_i$ are small. We omit the overline in $\overline{u}_i$ since all velocities displayed are mean values. Azimuthal velocities $u_\phi(r)$ are derived as a projection of the chordwise measurements $u_\chi(r)$ according to

$$u_\phi(r) = \frac{r}{e} u_\chi(r). \quad (14)$$

where $e = 25$ mm is the distance of the UDV chord (probe X) to the origin. We neglect the contribution of the radial component u_r, which is also contained in the u_χ-measurements, due to its small amplitude. Further support for this proceeding is given in Section V B.

Spatial average values over the measured UDV profiles are computed as

$$\langle u_\phi \rangle = \frac{\int u_\phi(r)\, r\mathrm{d}r}{\int r\mathrm{d}r} \quad (15)$$

and

$$\|u_r\| = \left(\frac{\int u_r^2(r,z)\, r\mathrm{d}r}{\int r\mathrm{d}r} \right)^{1/2}. \quad (16)$$

with $r \in [100, 150]$ mm in the core of the flow. The average azimuthal velocity $\langle u_\phi \rangle$ is used in the definition of the Reynolds number

$$Re = \frac{\langle u_\phi \rangle a}{\nu}. \quad (17)$$

Reynolds numbers reach $Re \approx 1.3 \cdot 10^4$ at $M = 2022$ in the steady regime considered in this paper.

IV. RESULTS

We now examine the data recorded in the laboratory experiment ZUCCHINI and the numerical simulations. As an example of the general dynamics in our setup at low forcing, Figure 3 shows the velocity field **u** from the numerics in a cross-section of the container at low forcing current and at two different values of the Hartmann number M (or the magnetic field strength B_0 respectively). The profile of the dominant azimuthal flow u_ϕ (colours) looks similar to hydrodynamic pipe flow at $M = 1$, whereas it is uniform along the direction of the magnetic field (axial) at $M = 200$. At the same time, the secondary flow gets concentrated in the boundary and free shear layers developing at large M. Figure 4 shows that the electrical current which drives the flow is flowing through the Hartmann and Shercliff layers, whereas the core is virtually current-free. At large M, most of the dissipation takes place in the thin Hartmann layers.

We start our presentation of the results with the order-one flow which is azimuthal due to the geometry of the Lorentz-forcing. Subsequently we study the secondary or recirculation flow in the (r, z)-plane before we turn to the boundary and internal shear layers.

A. Order-one flow

The azimuthal flow u_ϕ in our geometry is directly driven by the Lorentz force resulting from the radial current in an axial magnetic field. Figure 5a shows average values $\langle u_\phi \rangle$ from experiment and numerics. We observe a clear linear scaling with the electrical current, $\langle u_\phi \rangle \sim I$. Moreover the experimental data ($M > 35$) fall close to the same line as the numerical data with $M \geq 50$. The linear scaling $u_\phi \sim I$ is explained by a balance between the dissipation in the Hartmann layer and the driving by the Lorentz force.

The dashed line in Figure 5a indicates the theoretical value of $\langle u_\phi \rangle$ according to the basic model of Baylis and Hunt [12], further denoted as 'BH'. Averaging their expression for the azimuthal velocity in the core (Eq. 3)
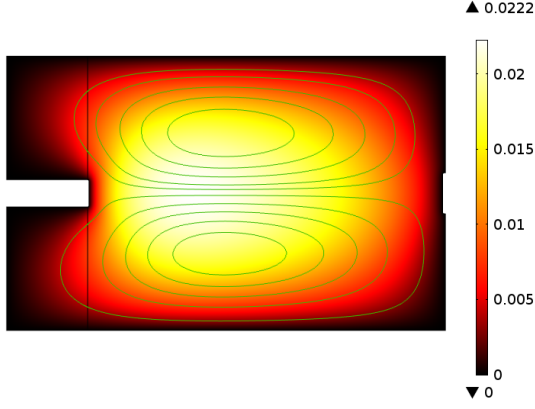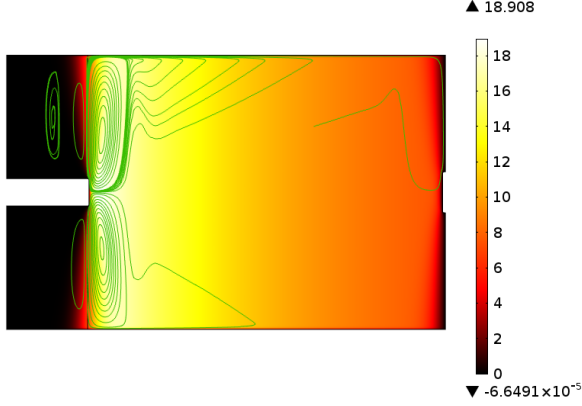
(a) $M = 1$, $I = 0.43$ mA

(b) $M = 200$, $I = 86.1$ mA

FIG. 3. Example of nondimensional velocity **u** in the numerical simulation with low forcing at (a) $M = 1$, $I = 0.43$ mA and (b) $M = 200$, $I = 86.1$ mA. The colour scale shows u_ϕ, the streamlines u_r and u_z.
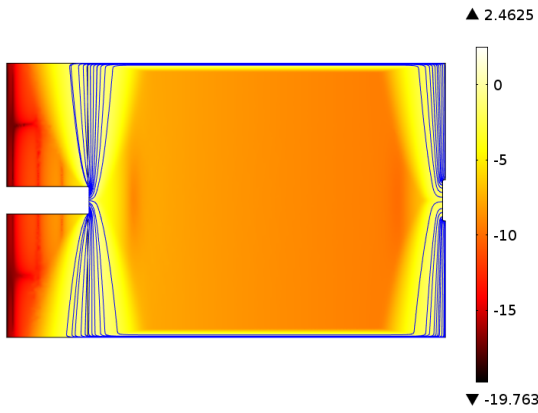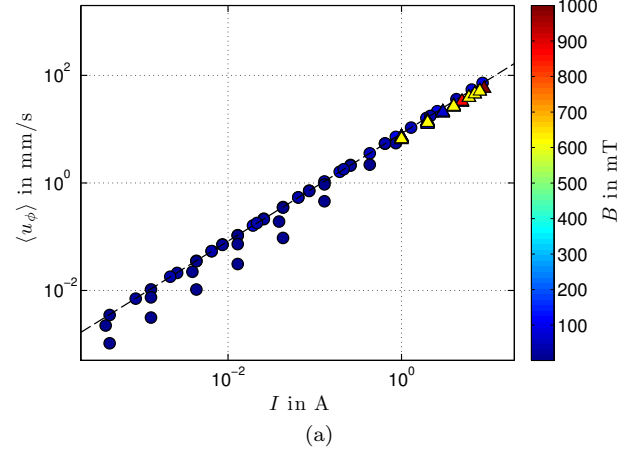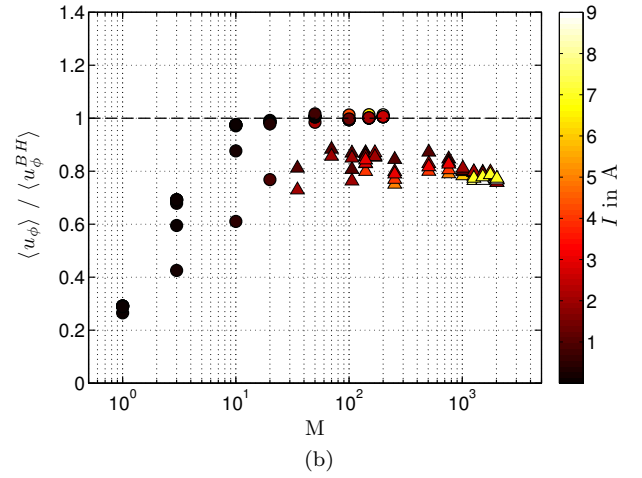

FIG. 4. Nondimensional electrical current density in the numerical simulation at $M = 200$, $I = 86.1$ mA (cf. Fig. 3b). The colour-coded quantity is $\log_{10}\mathbf{j}^2$ with streamlines of (j_r, j_z) superimposed to make the Hartmann and Shercliff layers visible which contain virtually the entire electrical current.

(a)

(b)

FIG. 5. Mean azimuthal flow $\langle u_\phi \rangle$ in experiment (triangles) and numerics (circles). Averages are taken along a radial beam with $r \in [100, 150]$ mm according to Eq. 15. (a) $\langle u_\phi \rangle$ scales linearly with the current I; the dashed line is the theoretical prediction $\langle u_\phi^{BH} \rangle$ from [12]. (b) $\langle u_\phi \rangle$ normalized by $\langle u_\phi^{BH} \rangle$ approaches the large-M limit for $M \gtrsim 50$.

according to Equation 15 between r_1 and r_2 leads to

$$\langle u_\phi^{BH} \rangle = \frac{I}{2\pi(r_2 + r_1)\sqrt{\sigma_e \rho \nu}}. \tag{18}$$

In Figure 5b, we observe a quantitative agreement within 25% between the theory and our experimental measurements for $M > 30$. Numerical simulations are shown to also converge toward the BH-value for $M > 30$. The azimuthal velocity $\langle u_\phi \rangle$ is observed to be independent of the Hartmann number M at large M as predicted by the BH-theory.

The UDV profiles of measured chordwise and derived azimuthal velocities, $u_\chi(r)$ and $u_\phi(r)$ are shown in Figure 6a and b, and compared with numerical and theoretical values. A characteristic feature is the velocity increase in the free shear layer due to the current injection at the edge of the inner disk electrode ($r_d = 75$ mm). The shear layer forms on the cylinder tangent to the inner
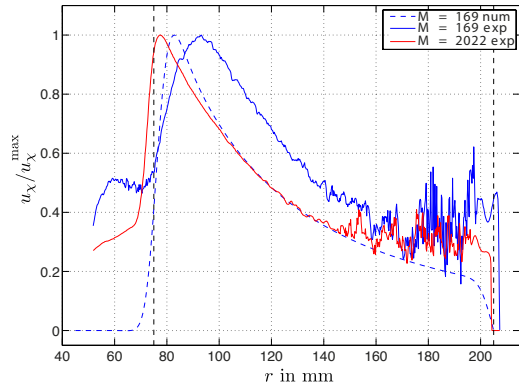
(a)
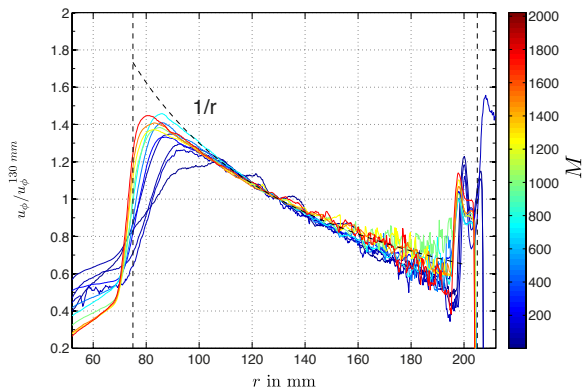
(b)

FIG. 6. Comparison of profiles of chordwise and azimuthal velocities in experiment (solid lines), numerics and theory for different M. (a) Chordwise profiles normalized to their maximum. The numerical profile for $M = 169$ (dashed) shows a greater shear at the inner electrode (dashed vertical line) than the experimental ones. (b) Derived azimuthal profiles (Eq. 14) normalized to their value at $r = 130$ mm. The dashed line depicts an algebraic law r^{-1}.

electrode, separating the flow into an electrically forced outer domain and an inner domain where the flow is entirely governed by the diffusion of momentum.

The chordwise velocities (Fig. 6a) exhibit a qualitative agreement between experimental and numerical data in the volume between the two electrodes (vertical lines), especially for $r \in [100, 150]$ mm. For large radii, the UDV signal is noisy. Above and below the inner electrode ($r < r_d$), we measure significant velocities in the experiment, whereas velocities in the numerical models vanish. The viscous entrainment appears to be higher in the experiment. This contributes to the fact that the shear in the free Shercliff layer at the inner electrode is greater in the numerical profiles. We will come back to this point in Section IV C.

The profiles of azimuthal velocity derived from experimental data (Fig. 6b) confirm the scaling $u_\phi(r) \sim r^{-1}$
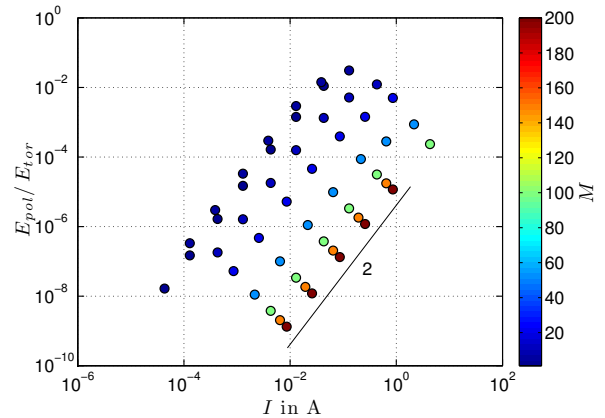
(a)
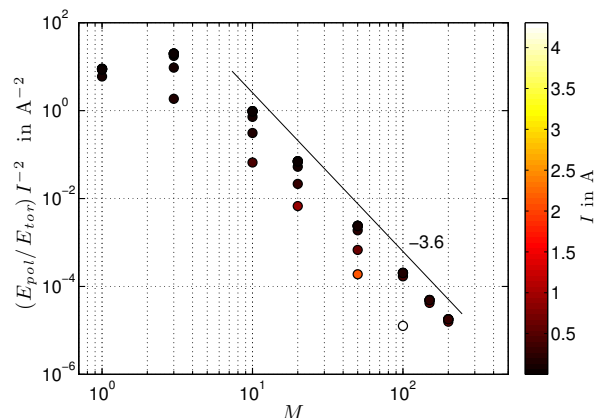
(b)

FIG. 7. Ratio of poloidal to toroidal kinetic energy integrated over the whole volume in numerical models displayed versus (a) the electrical current I and (b) the Hartmann number M. For large M, the ratio is very small and scales as $E_{pol}/E_{tor} \sim M^{-3.6} I^2$.

predicted by the BH-model (Eq. 3) between the electrodes. Significant deviations occur only near the inner electrode as an effect of the free shear layer. The scaling $u_\phi(r) \sim r^{-1}$ can be understood as the geometrical spreading of the forcing current in the Hartmann layer as $I \sim (2\pi r)^{-1}$.

B. Secondary flow

The dominant azimuthal flow in our setup drives a secondary recirculation in the (r, z)-plane. The magnitude of the secondary flow is much smaller than the one of the azimuthal flow. This is shown by the ratio of poloidal to toroidal kinetic energies, E_{pol}/E_{tor}, in the numerical models in Figure 7. Poloidal and toroidal kinetic energies are defined as $E_{pol} = 0.5 \iiint (u_r^2 + u_z^2)\, r\mathrm{d}r\mathrm{d}\phi\mathrm{d}z$ and $E_{tor} = 0.5 \iiint u_\phi^2\, r\mathrm{d}r\mathrm{d}\phi\mathrm{d}z$, respectively. E_{pol} reaches a few percent of E_{tor} at maximum, and decreases strongly
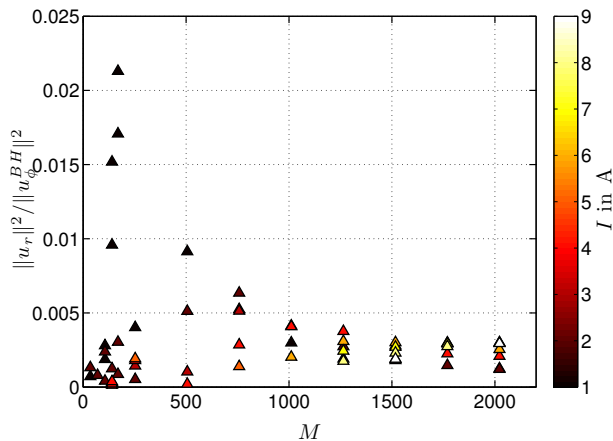
FIG. 8. The ratio of radial to azimuthal kinetic energy $\|u_r\|^2/\|u_\phi^{BH}\|^2$ displayed versus the Hartmann number M for the experimental data. The ratio does not decrease in the same way as in the numerical data (Fig. 7) in the large-M limit.
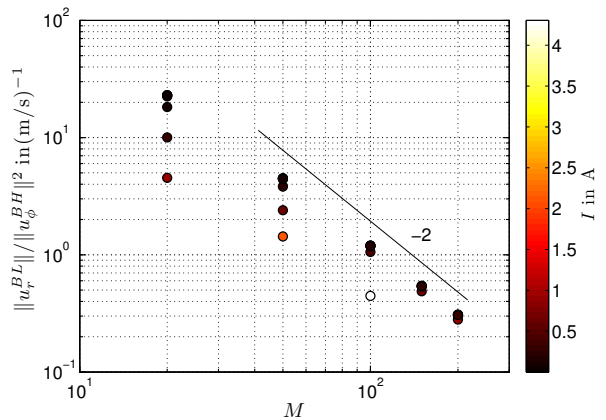

FIG. 9. Ratio of radial velocity in the boundary layers $\|u_r^{BL}\|$ to the square of the theoretical azimuthal velocity in the core $\|u_\phi^{BH}\|^2$. The observed scaling agrees well with the theory of [14]. It is not possible to extract comparable data for the experiment.

with M at large M. Also in the large-M, the ratio scales as $E_{pol}/E_{tor} \sim M^{-3.6}I^2$.

As seen from Figure 3, the recirculation flow in the (r, z)-plane has almost the same strength between inner and outer electrode at moderate $M = \mathcal{O}(1)$ in the numerical models. For large M, it is concentrated in the boundary and free shear layers. The two large recirculation cells ($z < 0$ and $z > 0$) present at moderate M break up into several cells when increasing M. The recirculation is largely suppressed in the core of the flow is as expected for this kind of quasi-2D flow.

In the experiment, the radial flow is probed by UDV probe R located 2.1 cm above the mid-plane of the tank. Hence we only have information on u_r in the core of the flow. We encounter radial velocities $\langle u_r \rangle$ that are again small compared to the order-one azimuthal flow as seen in Figure 8. In contrast to the numerical data, however, they preserve a finite magnitude up to the largest M. For most values of the electrical current, the ratio of radial to azimuthal kinetic energy $\|u_r\|^2/\|u_\phi^{BH}\|^2$ even appears to become constant above $M \approx 1000$. We will discuss the discrepancy in the radial flow between experiment and numerics in Section V.

C. Shear layers

1. Hartmann and Shercliff boundary layers

Hartmann and Shercliff boundary layers are the shear layers that form at walls perpendicular and parallel to the direction of the magnetic field to accommodate the core velocity to the non-slip boundary condition. At large M, their thicknesses scale as $\delta_H \sim M^{-1}$ and $\delta_S \sim M^{-1/2}$, respectively [4, 7]. Hence the theoretical boundary layers at the experimental values of $M \in [35, 2022]$ are as thin

as $\delta_H = [1.4, 0.02]$ mm and $\delta_S = [8.5, 1.1]$ mm. The observation of the outer wall Shercliff layer is hindered by spurious wall reflections and a low signal-to-noise ratio at large radii. For this reason, we only use the numerical models for the study of the boundary layers.

Figure 9 shows the ratio of the radial velocity averaged over all Hartmann and Shercliff layers to the square of the theoretical azimuthal velocity in the core. For large M, we observe a scaling as $\|u_r^{BL}\|/\|u_\phi^{BH}\|^2 \sim M^{-2}$. Since u_r is large only in the Hartmann layers, this relation is also found when integrating u_r over the whole volume or considering local measurements in the Hartmann layers only.

The observed scaling was also found in a theoretical study by Tabeling and Chabrerie [14] who studied pressure-driven MHD flow in an annular duct. The recirculation flow is driven by the main azimuthal flow u_ϕ. Tabeling and Chabrerie [14] derived that $u_r^{HL} \sim u_\phi^2 M^{-2}$ independent of the external driving.

Now we turn to the structure of the boundary layers. Figure 10a shows profiles of the velocity magnitude $u = (u_r^2 + u_\phi^2 + u_z^2)^{1/2}$ along z at the half-radius of the tank for different Hartmann numbers M. The velocity profile in the core of the flow is almost parabolic for $M = 1$ (hydrodynamic limit $M \to 0$), and becomes flatter with increasing M. For high magnetic fields ($M \gg 1$), the core flow is two-dimensionalized. Figure 10d shows the Hartmann layer thickness δ_H as a function of M (black circles). The thickness of the boundary layer is defined as the distance from the wall where the velocity magnitude u reaches 90% of its maximum (core) value. Fitting the data that have $M \geq 20$, the scaling found by linear regression is $\delta_H \sim M^{-1.003 \pm 0.004}$. This is in quantitative agreement with the theoretical scaling of M^{-1} for $M \gg 1$.
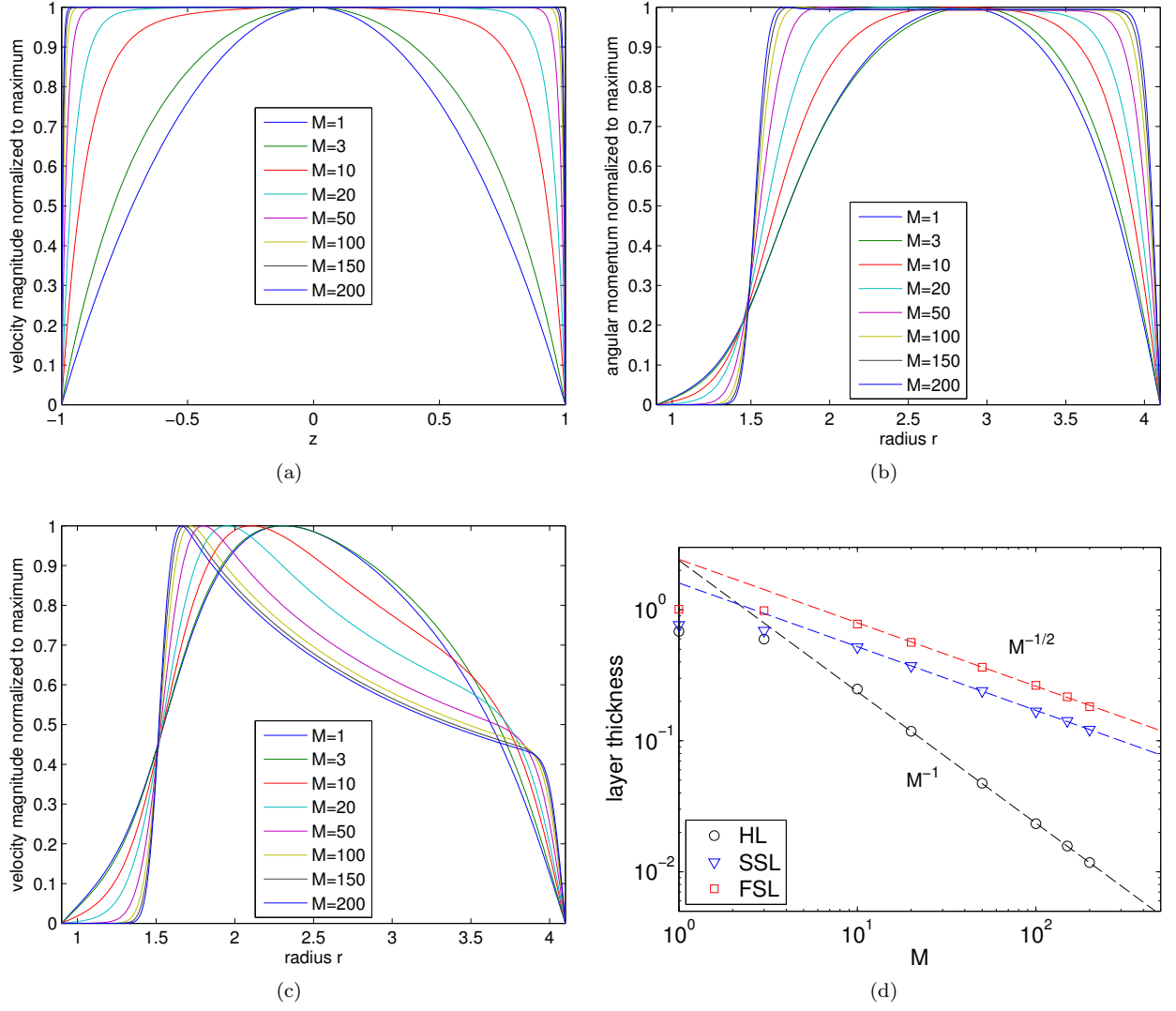
In our model, the boundary layer at the outer wall is

FIG. 10. Scaling of the Hartmann and Shercliff layers in the numerical models. (a) Profiles of the velocity magnitude $|u|$ normalized to its maximum value along the z-direction at the half-radius of the container for different Hartmann numbers M. (b) Profiles of the axial angular momentum $L = r \cdot u$ normalized to its maximum value along the r-direction at $z_i = 0.42$; the nondimensional height z_i is where the radial and chordwise UDV probes are located in the laboratory experiment. (c) Profiles of the velocity magnitude $|u|$ normalized to its maximum value along the r-direction at height z_i. (d) Scaling of the thickness of the Hartmann (HL), side (SSL) and free Shercliff (FSL) layers with the Hartmann number M.

not a typical side or parallel layer since only the central part of the outer cylinder is electrically conducting. In standard examples like Baylis and Hunt [12], the whole outer cylinder is conducting. For the computation of the wall Shercliff layer in the numerical data, we use the axial angular momentum profile $L = ru$ in Figure 10b since the velocity itself is known to drop off with the radius as in Equation 3. We again apply the 90%-criterion to the profile. The scaling for $M \geq 20$ is $\delta_S \sim M^{-0.486 \pm 0.007}$ (blue triangles in Fig. 10d) which is close to $\delta_S \sim M^{-1/2}$ from the geometrically simpler theoretical model. Hence the thicknesses of the boundary layers in the numerical models are in good agreement with the theoretical predictions.

2. Free Shercliff layer

Of particular interest is the free Shercliff layer extending vertically from the inner electrode. Figure 10c shows a radial profile of the velocity magnitude u which contains the free Shercliff layer at a nondimensional radius of $r = 1.5$. Similar to the Hartmann layer before, we define its thickness δ_S as the radial distance between 5% and 95% of the maximum velocity magnitude. Figure 10d shows the scaling of the free Shercliff layer thickness (red squares) as $\delta_S \sim M^{-0.485 \pm 0.009}$ agreeing well with the scaling $\delta_S \sim M^{-1/2}$ for parallel layers. The scaling exponent varies little when using different percentages in the criteria for the layer thicknesses.
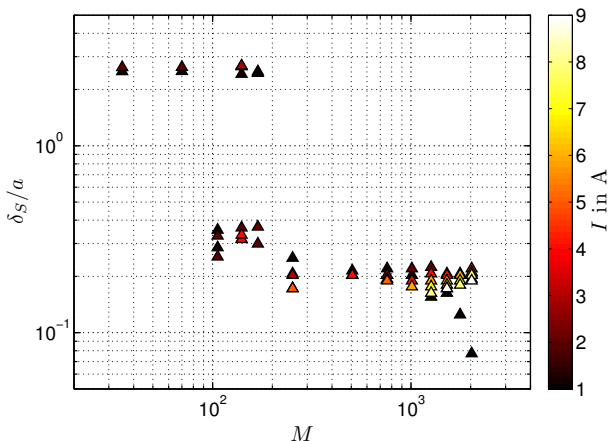
FIG. 11. Width δ_S of the free shear layer normalized by $a =$ 50 mm versus Hartmann number M. For currents $I > 1$ A, δ_S tends to a constant in the large-M limit.

As detailed above, it is difficult to measure the thin layer widths experimentally. For the free shear layer, however, it seems possible to extract a measure of the thickness from profiles as the ones in Figure 6. Defining the layer width as the distance between the maximum azimuthal velocity and the inner electrode $\delta_S = r(u_\phi^{max}) - r_d$ leads to Figure 11. We observe a lot of scatter in the data for moderate M. For large M, the layer width appears to become a constant of $\delta_S/a \approx 0.2$ which in dimensional units corresponds to roughly 10 mm. Only for a forcing current of 1 A, δ_S decreases further with M. This discrepancy between the inertialess theoretical and numerical scaling of $\delta_S \sim M^{-1/2}$ and the experimental measure is discussed in the next section.

V. DISCUSSION

The previous sections have shown a very good agreement of the dominant azimuthal flow in experiment, numerics and theory. The magnitude of the recirculation flow and the width of the free shear layer in the experiment, however, are much larger than expected from numerics and theory. In the following section, we discuss the differences between experiment and numerical model that might modify the flow in this way.

A. Axisymmetry numerics and experiment

The numerical model is perfectly axisymmetric and has a uniform axial magnetic field. Hence a crucial point is the degree of axisymmetry realized in the experiment which has implications for the reconstruction of the azimuthal velocity u_ϕ from the UDV measurements. Geometrically the laboratory setup is axisymmetric within negligible manufacturing tolerances. The

symmetry might, however, be broken by the electrical and magnetic setups.

The Lorentz-forcing of the flow in ZUCCHINI implies that the symmetry of the electrical current plays an important role. In the 'Caylar' setup, each of the three power supplies feeds two of the six segments of the outer ring electrode. The amount of current flowing through each segment is adjusted by additional Ohmic resistors to vary by less than 4% between segments. The copper electrodes have an electrical conductivity which is roughly 20 times higher than that of GaInSn. Hence we may assume a homogeneous distribution of the forcing current as long as wetting issues can be neglected.

A test of the sensitivity to the distribution of forcing current showed that the flow is not affected significantly even if one or more electrode segments are disconnected from the power supply as long as the remaining electrode distribution is reasonably symmetrical. In the 'Cryo' setup, we avoided the problem of uneven current distribution by using six power supplies, each feeding one segment of the outer electrode. Hence the electrical setup does not appear to be the cause of the observed discrepancies.

During installation in the 'Caylar' coil system, we centered the ZUCCHINI tank not only geometrically but also more precisely according to the magnetic field measurements. We mapped the magnetic field inside the coil volume by three perpendicular Hall effect sensors. With increasing radius, its magnitude decreases by 7% within the tank volume. Departures from axisymmetry were found to be negligible. However, there seemed to be a slight dependence of the field strength on the axial position with higher values in the lower part of the tank.

The 'Cryo' setup consists of a single superconducting coil made from twisted multi-filamentary NbTi/Cu by Cryomagnetics, Inc. As the magnetic field is generated by a single (short) coil, the magnetic field is less uniform than in the Helmholtz-type 'Caylar' setup. The 'Cryo' setup shows an increase in magnetic field strength with radius by roughly 15% and a significant amount of deviation from the axial direction at $z \neq 0$ near the outer cylinder. Also deviations from an axisymmetric field are larger than in the 'Caylar' setup.

B. Flow in the experiment

The order-one azimuthal flow u_ϕ is robust against small deviations from axisymmetry since it is directly driven by the interaction of the electrical current with the dominant axial field component. The radial flow u_r, however, appears to be quite sensitive to such deviations. In the case of non-axisymmetric magnetic fields, u_r is increased as observed in Figure 8 especially at large M ('Cryo' setup). This leads to an enhanced transport of angular momentum, resulting in a significant flow in the non-driven part of the fluid ($r < r_d$ in Fig. 6) and in a smoothing of the free shear layer (Fig. 11). Additionally

inertial effects may play a role at higher forcing. It appears that in most or all of the experimental profiles, we are not looking at the actual free Shercliff layer as in the numerics.

A second issue is the axisymmetry of the radial flow u_r itself. Comparing UDV measurements from probe R with the ones of probe X, which also contain u_r, we suspect that the radial flow is different at the two probe locations (cf. Fig. 2). Lacking complementary measurements, it is not possible to rigorously test this hypothesis. Nevertheless this observation together with the enhanced radial flow compared to the numerics has consequences for our data processing. In the reconstruction of azimuthal velocities u_ϕ (Eq. 14), we neglect the contribution $u_r \sqrt{r^2 - d^2}/d$ to the measured values u_χ. This approximation is justified since this contribution is small compared to $u_\chi r/d$ in the considered radial range. Figure 6 shows that the reconstruction of azimuthal velocities works well up to $r = 150$ mm where the noise in the data becomes significant.

VI.   CONCLUSION

We have studied the liquid metal flow that is generated by Lorentz-force driving in a modified cylindrical annulus by means of both laboratory experiments and numerical FE simulations. The peculiarity of the ZUCCHINI geometry compared to similar experimental studies [13, 20–22] is the inner electrode which is built as a disk protruding into the flow. This results in a free Shercliff layer between the inner and outer part without and with electrical forcing, which becomes unstable at currents of a few Amperes. This paper focuses on the steady axisymmetric base flow below this threshold.

Our experimental setup reaches Hartmann numbers M up to 169 for the 'Caylar' and 2022 for the 'Cryo' setup. The flow is probed by ultrasound Doppler velocimetry. To our knowledge, this is the first time, that the radial profile of electrically-driven azimuthal flow with a free Shercliff layer is established using UDV.

The structure of the base flow consists of a dominant azimuthal component and a secondary recirculation flow in the (r, z)-plane which is more than an order of a magnitude slower. The azimuthal flow is characterized by the inner non-driven part of the fluid, the free Shercliff layer, and a drop-off with increasing radius as $u_\phi(r) \sim r^{-1}$. We find very good agreement between the experimental data, the numerical results and the theoretical prediction from Baylis and Hunt [12]. The latter theory neglects secondary (radial and axial) flows and assumes large M. This large-M limit implies $u_\phi(r) \sim I$, which we observe in both numerical and experimental data, and appears to be reached for $M \gtrsim 30$ in our setup.

The secondary flow differs in its magnitude between experiment and numerics. A possible reason is the imperfect axisymmetry in the experimental setup. The enhanced radial angular momentum transport in the exper-

iment leads to a broadening of the free shear layer at the inner electrode. In the numerics, we observe the theoretically observed scaling of the Shercliff layer width as $\delta_S \sim M^{-1/2}$ from [7].

With this experimental and numerical study, we have established the base flow in ZUCCHINI which allows us to study the instabilities, especially the one of the free shear layer, in Paper 2.

Appendix A: Electrical boundary conditions

What are the appropriate electrical boundary conditions for the numerical simulations of ZUCCHINI? Imposing either the electric current density on or the voltage difference between the two electrodes leads to two different boundary conditions. Strictly speaking, neither of them is the one present in the lab experiment. There, the electrical current is kept fixed by controlling the voltage between the two electrodes. The electrical current density is free to rearrange on the electrodes while the potential difference between the two electrodes is not necessarily the same at all times. The corresponding boundary condition would be

$$\int_{\partial \Omega} \mathbf{j} \cdot \mathbf{n} \, dS = I_{imp}, \tag{A1}$$

where integration is performed over the conducting surface $\partial \Omega$ of the electrodes. It is, however, nonlocal and not straightforward implemented within a FE framework.

Instead, we choose to impose the current density j_0 at the inner electrode which leads to the dimensionless condition $-\nabla \Phi = \mathbf{e_r}$ (Neumann boundary condition for Φ). The outer electrode is set to ground, $\Phi = 0$ (Dirichlet boundary condition for Φ). At least on the outer electrode, the electrical current density is free to rearrange. Imposing j_0 on both electrodes appears to be physically impossible. All insulating walls have to fulfill the dimensionless electric boundary condition $\mathbf{n} \cdot \nabla \Phi = 0$.

Appendix B: Convergence study

We test the numerical convergence of our numerical model of ZUCCHINI by varying several parameters, especially the order of spatial discretization and the mesh. The parameters of the test case are $M = 202.22$ and $Re_i = 114.86$. These numbers correspond to the highest magnetic field that can be reached in the 'Caylar' setup ($B_{max} = 0.1$ T), and an electrical current density j_0 that is based on an imposed current of 1 A on the inner electrode which in the experiment yielded a steady flow at first sight.

On the one hand we vary the order of spatial discretization. For velocity, we test P3 (cubic) and P2 (quadratic), for pressure P2 and P1 (linear), for the electric potential quintic, quartic and quadratic. Also we study the
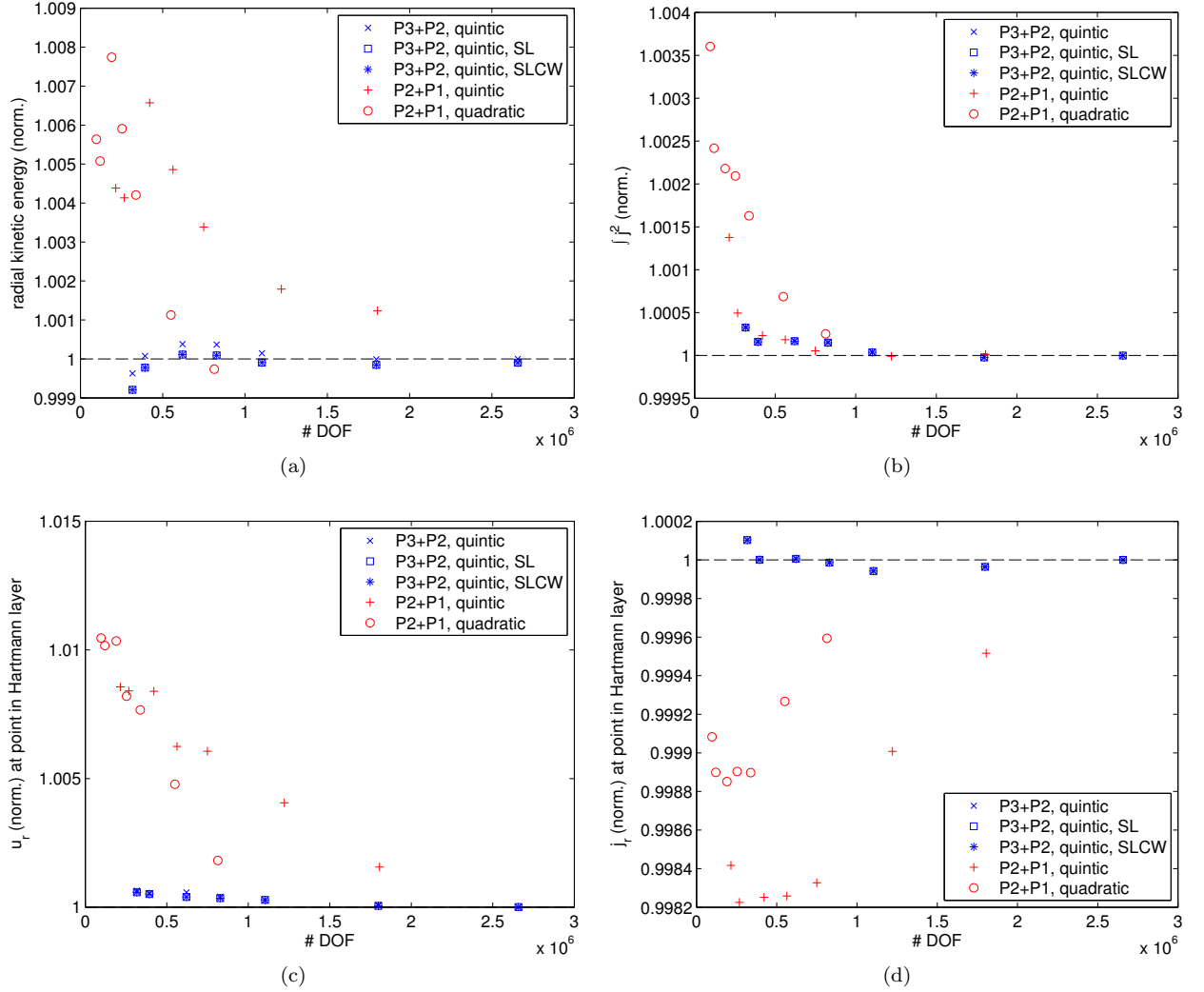
FIG. 12. Convergence of global and local quantities. (a) Radial kinetic energy when decreasing the element size in the mesh. (b) 'Ohmic dissipation'. (c) Radial velocity u_r in the Hartmann layer. (d) Radial current density j_r in the Hartmann layer. Results are normalized by the best-resolved 'P3+P2, quintic' simulation.

effects of streamline diffusion (SL) and crosswind diffusion (CW) which damp numerical oscillations by adding a small amount of artificial diffusion in the streamwise and crosswind direction respectively. On the other hand we parametrize the element size, resulting in meshes with different numbers of degrees of freedom (DOF).

Convergence is assessed using several global and local quantities derived from velocity and current density. Besides we also test whether the divergence-free conditions for velocity and current density are fulfilled globally and locally. Examples of the convergence of global quantities are given in Figures 12a and b which show integrated radial kinetic energy $E_r = 0.5 \int u_i^2 dS$ and integrated 'Ohmic dissipation' $\int (j_r^2 + j_\phi^2 + j_z^2) dS$. Figures 12c and d display the convergence of point measurements of u_r and j_r in the Hartmann layer. All quantities are normalized to the best-resolved simulation with discretization 'P3+P2, quintic'. In conclusion of this first part

of the convergence study, we choose to use discretization 'P3+P2, quintic' with streamline diffusion. A model with roughly 10^6 DOF is observed to have a sufficient numerical convergence that is better than 0.1%.

In the second step of our convergence study, we refine the element size of the mesh in the core and the boundary layers independently from each other. It turns out that by decreasing boundary layer size, we improve convergence further, whereas decreasing core element size does not make a difference. In general we make sure that the boundary and shear layers are resolved by at least 5 elements within their thickness [31].

The quantity most difficult to conserve is $\nabla \cdot \mathbf{j} = 0$. In our study, we only use simulations that have a ratio of inflowing over outflowing electrical current of $I_{in}/I_{out} \in [95\%, 105\%]$. This criterion discards the models with the largest forcing current for $M \geq 100$, and leaves us with 51 out of 56 models.

ACKNOWLEDGMENTS

[1] J Larmor, "Possible rotational origin of magnetic fields of sun and earth," Electrical Review **85**, 412ff. (1919).

[2] P Olson, "8.01 Overview," Treatise on Geophysics **8 Core Dynamics**, 1–30 (2007).

[3] R Moreau and S Molokov, "Magnetohydrodynamics - Historical Evolution and Trends," (Springer, 2007) Chap. Julius Hartmann and His Followers: A Review on the Properties of the Hartmann Layer, pp. 155–170.

[4] J Hartmann, "Hg-dynamics I: Theory of the laminar flow of an electrically conductive liquid in a homogeneous magnetic field," Mathematisk-fysiske Meddelelser, Det Kgl. Danske Videnskabernes Selskab **XV**, 1–28 (1937).

[5] J Hartmann and F Lazarus, "Hg-dynamics II: Experimental investigations on the flow of mercury in a homogeneous magnetic field," Mathematisk-fysiske Meddelelser, Det Kgl. Danske Videnskabernes Selskab **XV**, 1–45 (1937).

[6] PA Davidson, *An Introduction to Magnetohydrodynamics* (Cambridge University Press, 2001).

[7] J Shercliff, "Steady motion of conducting fluids in pipes under transverse magnetic fields," Mathematical Proceedings of the Cambridge Philosophical Society **49**, 136–144 (1953).

[8] JCR Hunt, "Magnetohydrodynamic flow in rectangular ducts," Journal of Fluid Mechanics **21**, 577–590 (1965).

[9] JCR Hunt and K Stewartson, "Magnetohydrodynamic flow in rectangular ducts. II," Journal of Fluid Mechanics **23**, 563–581 (1965).

[10] J Hunt and W Williams, "Some electrically driven flows in magnetohydrodynamics. Part 1. Theory," Journal of Fluid Mechanics **31**, 705–722 (1968).

[11] JA Baylis, "Detection of the onset of instability in a cylindrical magnetohydrodynamic flow," Nature **204**, 563 (1964).

[12] J Baylis and J Hunt, "MHD flow in an annular channel; theory and experiment," Journal of Fluid Mechanics **48**, 423–428 (1971).

[13] J Baylis, "Experiments on laminar flow in curved channels of square section," Journal of Fluid Mechanics **48**, 417–422 (1971).

[14] P Tabeling and J Chabrerie, "Magnetohydrodynamic secondary flows at high hartmann numbers," Journal of Fluid Mechanics **103**, 225–239 (1981).

[15] DS Krasnov, E Zienicke, O Zikanov, T Boeck, and A Thess, "Numerical study of the instability of the Hartmann layer," Journal of Fluid Mechanics **504**, 183–211 (2004).

[16] S Vantieghem and B Knaepen, "Numerical simulation of magnetohydrodynamic flow in a toroidal duct of square cross-section," International Journal of Heat and Fluid Flow **32**, 1120–1128 (2011).

[17] Y Zhao and O Zikanov, "Instabilities and turbulence in magnetohydrodynamic flow in a toroidal duct prior to transition in Hartmann layers," J. Fluid Mech. **692**, 288–316 (2012).

[18] IV Khalzov, AI Smolyakov, and VI Ilgisonis, "Equilibrium magnetohydrodynamic flows of liquid metals in magnetorotational instability experiments," Journal of Fluid Mechanics **644**, 257–280 (2010).

[19] A Potherat, J Sommeria, and R Moreau, "An effective two-dimensional model for MHD flows with transverse magnetic field," Journal of Fluid Mechanics **424**, 75–100 (2000).

[20] P Moresco and T Alboussiere, "Experimental study of the instability of the Hartmann layer," J. Fluid Mech. **504**, 167–181 (2004).

[21] J Boisson, A Klochko, F Daviaud, V Padilla, and S Aumaitre, "Travelling waves in a cylindrical magnetohydrodynamically forced flow," Phys Fluids **24**, 044101 (2012).

[22] B Mikhailovich, A Shapiro, S Sukoriansky, and I Zilberman, "Experiments with turbulent rotating MHD flows in an annular gap," Magnetohydrodynamics **48**, 43–50 (2012).

[23] K Messadek and R Moreau, "An experimental investigation of MHD quasi-two-dimensional turbulent shear flows," J. Fluid Mech. **456**, 137–159 (2002).

[24] R Hollerbach, X Wei, J Noir, and A Jackson, "Electromagnetically driven zonal flows in a rapidly rotating spherical shell," Journal of Fluid Mechanics **725**, 428–445 (2013).

[25] NB Morley, J Burris, LC Cadwallader, and MD Nornberg, "GaInSn usage in the research laboratory," Review of Scientific Instruments **79**, 056107 (2008).

[26] F Stefani, T Gundrum, G Gerbeth, G Rüdiger, M Schultz, J Szklarski, and R Hollerbach, "Experimental evidence for magnetorotational instability in a Taylor-Couette flow under the influence of a helical magnetic field," Phys. Rev. Lett. **97**, 184502 (2006).

[27] *DOP3000 series User's manual*, Signal Processing S.A., www.signal-processing.com, software 4.01 ed.

[28] D Brito, HC Nataf, P Cardin, J Aubert, and JP Masson, "Ultrasonic Doppler velocimetry in liquid gallium," Exp Fluids **31**, 653–663 (2001).

[29] A Cramer, C Zhang, and S Eckert, "Local flow structures in liquid metals measured by ultrasonic Doppler velocimetry," Flow Measurement and Instrumentation **15**, 145–153 (2004).

[30] O Andreev, Y Kolesnikov, and A Thess, "Application of the ultrasonic velocity profile method to the mapping of liquid metal flows under the influence of a non-uniform magnetic field," Exp Fluids **46**, 77–83 (2009).

[31] T Tagawa, G Authie, and R Moreau, "Buoyant flow in long vertical enclosures in the presence of a strong horizontal magnetic field. Part 1. Fully-established flow,"

European Journal of Mechanics - B/Fluids **21**, 383–398 (2002).